Drug Design, Development and Therapy

Dovepress
Taylor & Francis Group

Open Access Full Text Article

ORIGINAL RESEARCH

pH-Sensitive Porphyrin Metal-Organic Frameworks for Controlled Delivery of Para-Toluenesulfonamide and Photodynamic Cancer Therapy

Wei Zhou[1], Fan Feng[2], Jieli Zhang[3], Shuang Cao[4], Yunzhi Zhou[3], Yanming Li[1]

[1]Department of Pulmonary and Critical Care Medicine, Beijing Hospital, National Center of Gerontology, Institute of Geriatric Medicine, Chinese Academy of Medical Science, Beijing, 100730, People's Republic of China; [2]Clinical Laboratory, The Fifth Medical Center of Chinese People's Liberation Army General Hospital, Beijing, 100039, People's Republic of China; [3]Department of Respiratory and Critical Care Medicine, Emergency General Hospital, Beijing, 100028, People's Republic of China; [4]School of Chemical Engineering and Pharmacy, Wuhan Institute of Technology, Wuhan, 430205, People's Republic of China

Correspondence: Yanming Li, Department of Pulmonary and Critical Care Medicine, Beijing Hospital, National Center of Gerontology, Institute of Geriatric Medicine, Chinese Academy of Medical Science, Beijing, 100730, People's Republic of China, Email liyanming2632@bjhmoh.cn; Yunzhi Zhou, Department of Respiratory and Critical Care Medicine, Emergency General Hospital, Beijing, 100028, People's Republic of China, Email zhouyunzhi2017@126.com

Introduction: Photodynamic therapy (PDT) is a promising approach for tumor treatment. PDT for treating lung squamous cell carcinoma (LSCC) under the guidance of bronchoscopy has great potential for development. However, the use of high-intensity lasers in treatment may pose a risk of tissue damage. To address this issue, enhancing the sensitivity of tumor tissue to phototherapy is highly valuable.

Methods: In this study, a simple method was employed to prepare porphyrin-metal framework nanoparticles (NPs), referred to as HA-PTS@PCN. The design of these NPs is based on the concept of tumor sensitization, constructed with the porphyrin-based metal-organic framework compound PCN-224 to load the drug para-toluenesulfonamide (PTS).

Results: Multiple experiments have demonstrated that these NPs can be effectively absorbed and selectively release PTS within the acidic tumor microenvironment. Under 660 nm laser irradiation, the material releases reactive oxygen species, demonstrating effective photodynamic therapeutic effects. Additionally, due to the tumor-sensitizing properties of PTS, the treatment efficacy of these NPs on LSCC is significantly greater than that of PCN-224 alone. Both in vitro and in vivo studies confirmed that combining tumor sensitization strategies with PDT therapy for LSCC significantly enhances anticancer effects.

Discussion: This study provides a universal strategy for preparing drug-loaded PDT nanoplatforms and offers a new approach for developing nanomedicine with tumor-sensitizing effects.

Keywords: PTS, metal-organic framework, tumor sensitization, nanomedicine, PDT

Introduction

Lung cancer is the leading cause of cancer-related deaths, representing 20.4% of all cancer fatalities. The National Cancer Institute (https://seer.cancer.gov) estimates that there will be 125,000 lung cancer deaths in the United States in 2024.[1] Lung cancer is mainly classified into two types: small cell lung cancer and non-small cell lung cancer (NSCLC), with NSCLC making up about 85% of cases. The most common subtypes of NSCLC are lung adenocarcinoma and LSCC, with LSCC comprising around 30% of NSCLC cases.[2,3] Approximately one-third of patients with LSCC are already in the advanced stage at the time of diagnosis, making surgery no longer feasible.[3,4] Over the past two decades, treatment has shifted from traditional cytotoxic therapy to more targeted and better-tolerated options.

PDT is an emerging cancer treatment that utilizes lasers of specific frequencies to activate photosensitizing agents, which release reactive oxygen species (ROS) such as singlet oxygen, hydroxyl radicals, superoxide, and hydrogen peroxide ($^1O_2$,

Received: 9 December 2024
Accepted: 11 March 2025
Published: 1 April 2025

Graphical Abstract

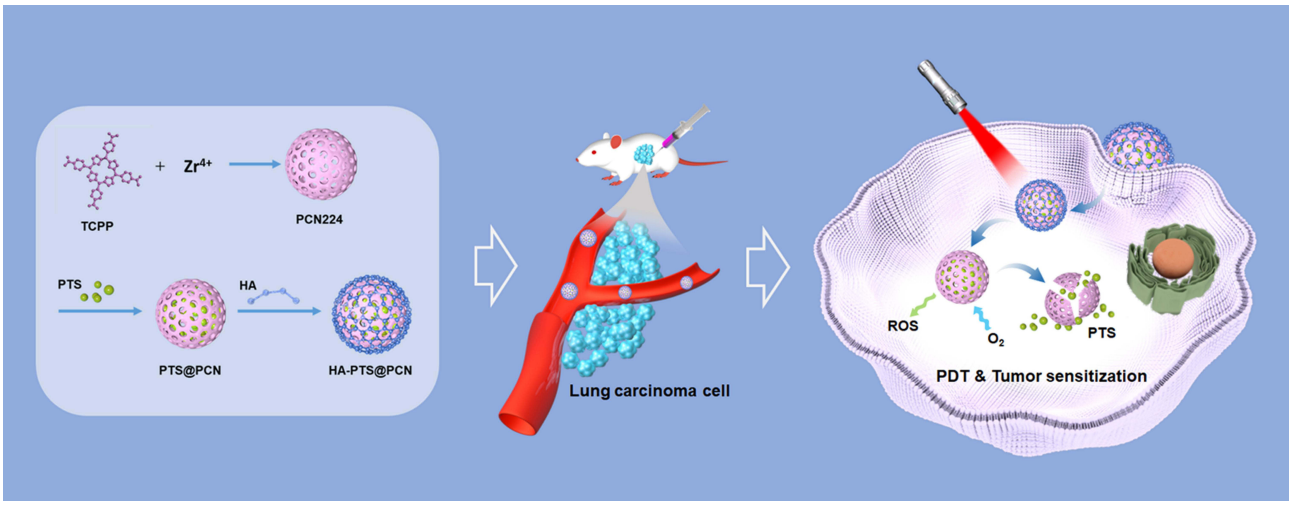

OH, O^{2-}, and H_2O_2) to inhibit cancer cell growth. PDT is characterized by its minimal invasiveness, low toxicity, and high selectivity. Numerous clinical trials have been reported, demonstrating the efficacy of PDT in the treatment of various diseases, including actinic keratosis, esophageal cancer, and skin cancer.[5–10] However, it has been primarily effective for superficial tumors and considerably less so for deeper-seated tumors.[11–13] Common methods to boost PDT efficacy, such as increasing laser power and exposure time, pose risks of laser burns to the skin. How to obtain a safer and more effective PDT is the focus of current research. Various sensitization strategies are available for other antitumor therapeutic strategies, including antitumor drug therapy, radiation therapy, and interventional therapy, but no PDT sensitization has been reported. In this study, we aim to use PTS as a sensitizer to enhance tumor sensitivity and improve PDT efficacy.[14–17]

PTS is a lipophilic drug that inhibits the Akt/mTOR/p70S6K pathway.[18–23] Multiple studies have shown that PTS can enhance the sensitivity of chemotherapy and radiotherapy, making it a viable option for use as an adjuvant in local and intratumoral injections alongside chemotherapy and radiotherapy.[24] Li et al reported a Phase III clinical trial, which confirmed that PTS shows certain efficacy and tolerability in the treatment of NSCLC with severe airway obstruction. It can significantly relieve airway obstruction, improve pulmonary function and quality of life, and prolong patient survival.[25,26] However, there are still some pressing issues that need to be addressed in the clinical application of PTS. For instance, the tumor-suppressing ability of PTS is limited, and it can only demonstrate its efficacy against tumors when administered at higher doses. This is primarily due to the rapid metabolic rate of PTS, which prevents it from maintaining high concentrations within the tumor for an extended period.

To address the aforementioned issue, this research project combines PTS and PDT for the first time, aiming to achieve sustained release of PTS and enhance the therapeutic efficacy of PDT. We synthesized a metal-organic framework (MOF) material based on a porphyrin structure (PCN-224) (Figure 1). Subsequently, the PTS was loaded into PCN-224 and coated with hyaluronic acid (HA). This material exhibits photodynamic properties, capable of releasing reactive oxygen species (ROS) upon irradiation with a laser of a specific wavelength. Additionally, it can slowly release PTS in the acidic tumor microenvironment, sensitizing the tumor tissue and enhancing the efficacy of PDT.

Materials and Methods

Materials and Reagents

Zirconyl chloride octahydrate ($ZrOCl_2 \cdot 8H_2O$, 98%), benzoic acid (99.5%), hyaluronic acid (HA), tetrakis (4-carboxyphenyl) porphyrin (TCPP, 97%), 1,3-diphenylisobenzofuran (DPBF, 97%), and 2.7-dichlorodihydrofluorescein diacetate (DCFH-DA, 97%) were purchased from Bidepharm Co., Ltd (Shanghai, China). The ROS detection kit and Annexin

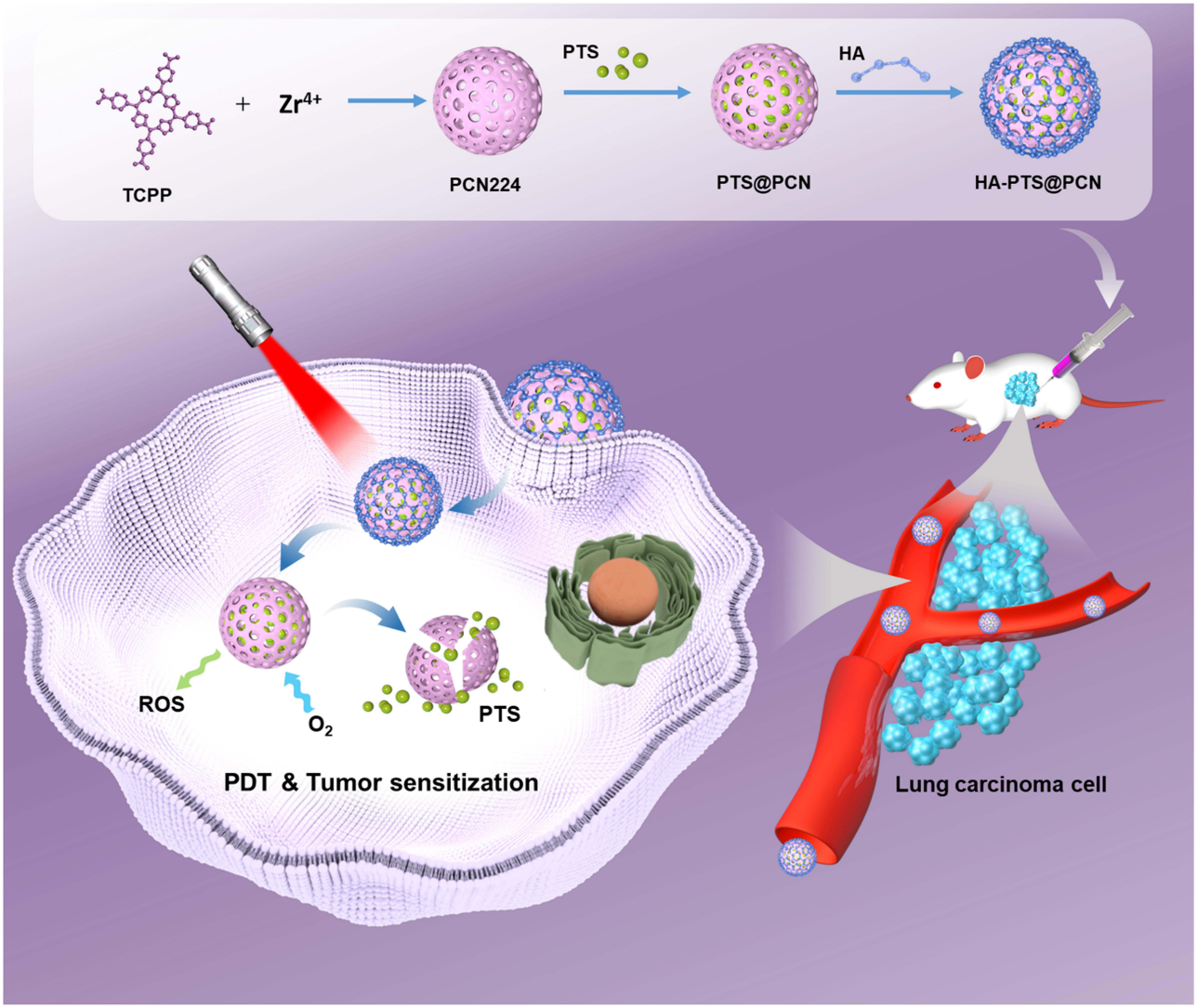

Figure 1 Schematic diagram of the preparation of HA-PTS@PCN NPs and the mechanism of using these NPs for synergistic PDT. The preparation of HA-PTS@PCN NPs involves three steps: the synthesis of PCN-224, the loading of PTS, and coating with HA. After an intravenous injection into tumor-bearing mice, HA-PTS@PCN NPs can slowly release PTS in the mildly acidic environment of the tumor region. PTS activates the AKT signaling pathway, enhancing the sensitivity of tumor cells to PDT treatment, thereby further improving the therapeutic efficacy of PDT. Therefore, HA-PTS@PCN NPs, as an effective PDT sensitizer, synergistically enhance the tumor inhibition effect in tumor PDT treatment.

V-FITC/PI apoptosis detection kit were also obtained from Bidepharm Co., Ltd (Shanghai, China). The Calcein-AM/PI Double Stain Kit was purchased from Solarbio Biotechnology Co., Ltd (Beijing, China). All chemical reagents were used as received without further purification. Human lung squamous carcinoma cells (NCI-H520) were obtained from the Cell Bank of the Chinese Academy of Sciences (Shanghai, China). These cells were cultured in RPMI-1640 medium (Invitrogen, USA), supplemented with 10% (V/V) fetal bovine serum (FBS, Invitrogen, USA), at 37°C in a 5% CO_2 atmosphere.

Synthesis of PCN-224 NPs

20 mg of TCPP, 60 mg of $ZrOCl_2 \cdot 8H_2O$, and 800 mg of benzoic acid were added into a reaction vessel. The mixture was dissolved in 4 mL of DMF with ultrasonic treatment until fully dissolved. The reaction was carried out at 90°C for 24 hours. After cooling to room temperature, the mixture was centrifuged, and the precipitate was washed three times with ethanol and vacuum-dried to obtain nanoscale PCN-224.[27–29]

https://doi.org/10.2147/DDDT.S504891

Preparation of PTS@PCN NPs

The synthesized PCN-224 NPs (5 mg/mL, 10 mL) were added to a DMSO solution of PTS (30 mg/mL, 10 mL). The mixture was stirred at room temperature for 48 hours. It was then centrifuged for 20 minutes, washed three times with methanol, and dried to obtain PTS-loaded PCN-224 NPs, designated as PTS@PCN. The amount of free PTS in the supernatant was determined using high-performance liquid chromatography (HPLC), and the drug loading capacity (DLC) was calculated according to the following formula: DLC (%) = [(Weight of loaded PTS)/(Weight of PCN224)] × 100%.[30,31]

Preparation of HA-PTS@PCN NPs

Disperse 20 mg of PTS@PCN in 10 mL of an ethanol solution of HA (20 mg/mL) and stir rapidly for 40 minutes. Then, obtain HA-PTS@PCN by centrifugation and drying at room temperature, as described in reference. HA@PCN nanoparticles were prepared using a similar method.

Drug Release Process Test

10 mg of HA-PTS@PCN NPs were dispersed in 40 mL of PBS (10 mm), and 0.04 mL of Tween 80 was added. The pH of the solution was adjusted to 5.5 or 7.4, and then irradiated with a 660 nm laser (100 $mW \cdot cm^{-2}$, 5 minutes). The control group was kept in the dark. The temperature of the solution was maintained at 37°C and stirred at a constant speed of 75 revolutions per minute. Subsequently, within 72 hours, 0.1 mL of the medium was taken every 12 hours as a detection sample. The samples were centrifuged at 10,000 revolutions per minute for 10 minutes. The supernatant was then analyzed by HPLC to plot the PTS release curve.

In vitro Detection of ROS

Using DPBF as a chemical probe to detect the production of $^1O_2$. In brief, various prepared NPs were mixed with a DMSO solution containing 10 μg/mL DPBF. The mixture was then irradiated under a 660 nm laser (100 mW/cm^2) for 5 minutes, and the absorbance of the DPBF solution at 415 nm was measured every 2 minutes. A DPBF solution served as the control. The testing method for HA-PTS@PCN was the same as for PCN-224 NPs, except that the reaction medium was changed from DMSO to methanol.

To detect ROS production using DCFH-DA, add DCFH-DA (10 μmol/L) to the different NPs solution. Expose the mixture to a 660 nm laser for 5 minutes, then measure the absorbance of the DCFH-DA solution at 525 nm every 2 minutes. Use a pure DCFH-DA solution as the control sample.[32]

Production and Measurement of Intracellular ROS

H520 cells were incubated with PBS and various NP solutions for 24 hours. After the incubation, the cell culture medium was removed.[33–36] The cells were then incubated with DCFH-DA (10 μmol/L) for 2 hours, washed, and irradiated with a 660 nm (100 mW/cm²) laser for 5 minutes. Ten minutes later, the fluorescence intensity of DCF was observed using a confocal laser scanning microscope (CLSM, Olympus IX71, excitation/emission: 488/525 nm).[29,37] For the control group, cells were treated with PBS solution and irradiated with a 660 nm (100 mW/cm²) laser for 5 minutes.

Colony Formation Assay

H520 cells are cultured in a complete medium composed of 90% DMEM and 10% fetal bovine serum. After seeding the cells in a 6-well cell culture plate and allowing them to reach 80%-90% confluence, PTS, PCN-224, PTS@PCN, and HA-PTS@PCN were added at concentrations of 20 μg/mL, 14.5 μg/mL, 34.5 μg/mL, and 34.5 μg/mL, respectively, to each well under dark conditions. Incubate in a 37°C incubator for 24 hours, then irradiation was performed with a laser (660 nm, 100 mW/cm²) for 5 minutes. After laser treatment, the cells were incubated for approximately 12 hours. Subsequently, the cells were gently digested with trypsin, and they were reseeded in a 6-well plate at a seeding density of 800 cells per well. After seeding, the plate was placed back in the incubator. The cell status was observed daily, and the medium was changed every 3–5 days. After 2–4 weeks of growth, once colonies formed, the cell colonies were stained

with a solution containing 0.5% crystal violet and 25% methanol. For the control group, the cells were treated with PBS solution, and irradiated was performed with a 660 nm (100 mW/cm²) laser for 5 minutes.

Flow Cytometry Analysis

The medium containing PBS, PTS, PCN-224, PTS@PCN, and HA-PTS@PCN was incubated for 24 hours. Following laser irradiation (660 nm, 100 mW/cm²) for 5 minutes, the cells were incubated for an additional 24 hours, and then they were collected by centrifugation. They were incubated in a binding buffer containing 5 μL of Annexin-V FITC and 10 μL of propidium iodide (PI) for 10 minutes. The signals were collected using a BD FACS Calibur flow cytometer (Beckman/Gallios). Annexin V-FITC was detected through the FITC Detection Channel (excitation: 488 nm; emission: 530 nm) and PI was detected by PI Detection Channel (excitation: 535 nm; emission: 615 nm).

Cell Staining Experiment

The cells were incubated in media containing PBS, PTS, PCN-224, PTS@PCN, and HA-PTS@PCN for 24 hours. After laser irradiation (660 nm, 100 mW/cm²) for 5 minutes, they were incubated for another 24 hours, and then the cells were collected by centrifugation. Using the Calcein-AM/PI assay kit, 1–2 μL of Calcein-AM stock solution was added to each 1 mL of cell suspension (1×10^6 cells/mL), after which the solution was mixed well and incubated at 37°C in the dark for 20 minutes. Subsequently, 4 μL of the PI stock solution was added to the stained cells and incubated at room temperature in the dark for 5 minutes. The fluorescence of the cells was observed under a fluorescence microscope (Olympus, IX71), and photographs were captured.[37]

Western Blot Experiment

After pretreating H520 cells with PTS, PCN-224, PTS@PCN, and HA-PTS@PCN for 24 hours, the cells were exposed to laser irradiation and then incubated for an additional 24 hours. Following this exposure, the cells from each group were collected and lysed in RIPA buffer (Cell Signaling Technology, Danvers, MA, USA) to extract total protein. Protein concentration was determined using the Pierce bicinchoninic acid protein assay kit (Thermo Fisher Scientific, Inc). The protein samples were then separated using sodium dodecyl sulfate-polyacrylamide gel electrophoresis (Millipore, Billerica, USA). Subsequent steps included membrane transfer, blocking, and antibody incubation. β-Actin served as the internal control, and primary antibodies used were phospho-P70S6K (Thr389), P70S6K, phospho-AKT (Ser473), AKT, phospho-mTOR (Ser2448), mTOR, and β-actin, with horseradish peroxidase-conjugated IgG as the secondary antibody. All antibodies were obtained from Cell Signaling Technology (Danvers, MA, USA).[38,39] In the control group, cells were treated with PBS solution and irradiated with a 660 nm laser (100 mW/cm²) for 5 minutes.

Animal Experiments

The biological activity of the candidate compounds was assessed in vivo using a nude mouse model. The experimental design and the protocol for animal-related experiments, which were conducted in accordance with the UK Animals Act, 1986 (Scientific Procedures) guidelines, were reviewed and approved by the Institutional Animal Care and Usage Committee of the fifth medical center of Chinese people's liberation army general hospital (Approval ID: IACUC-2021-0026).

In vivo Pharmacodynamic Evaluation

H520 cells (5×10^6 cells) were subcutaneously injected into the nude mice. Treatment began when the tumors grew to approximately 700–1000 mm³ (around the 4th week). The drug was injected into the tumor tissue, and after avoiding light for 4 hours, laser irradiation was performed. Tumor volume was measured using a Vernier caliper at 0, 2, 4, 6, 8 and 9 week post-inoculation. Tumor volume was estimated using the formula: Tumor volume V = (l)×(w)×(w)/2, where l is the tumor length and w is the tumor width. The control group received an injection of only PBS solution. The dosage of NPs (HA-PTS@PCN and PTS@PCN) is 10 mg/kg, and the dosage of PTS is 5.8 mg/kg. After treatment, the mice were euthanized, and tumor tissues from each group were collected. The tissues were quickly frozen in liquid nitrogen after segmentation for subsequent biochemical analysis.

In vivo Distribution of NPs and Stimuli-Responsive Release Profile Within Tumors

In this study, we determined the metabolic rate of PTS in tumor tissues and blood for several types of NPs. The metabolism or clearance of PTS in tumor tissues formed by H520 cells was measured using LC-MS. Following the injection of HA-PTS@PCN and PTS@PCN NPs into the subcutaneous tumor tissues of nude mice, intravenous whole blood and tumor tissues were collected from each group at different time points. Liquid nitrogen was then added to the tumor tissues for grinding. Subsequently, the tissue samples were resuspended in sterile PBS, and an equal volume of the organic solvent acetonitrile was added. After vortexing to homogenize the tissue samples, the drug PTS was extracted into the acetonitrile. The content of PTS in the cell samples at different time points was detected by LC-MS.[40,41] Once the intravenous whole blood had settled adequately, plasma was collected to determine the blood drug concentration-time curve.

Research on Biochemical and Metabolic Characteristics

This study utilized quantitative polymerase chain reaction (qPCR) to assess metabolism-related factors in tumor tissues treated with NPs. The drug was administered either alone or combined with laser treatment to subcutaneous tumors. Subcutaneous tumor tissues were then harvested, total RNA was extracted, reverse transcribed, and analyzed using one-step qPCR, as outlined in the literature.[42] For qPCR data analysis, the relative expression level of the control group was set as the baseline "1". The fold changes between each group and the control group were calculated, and heat maps were generated following established methods.[43] The color scale of the heat map indicates variations relative to the control group.

The tested gene panel included factors related to cell cycle regulation, such as Cyclin B, Cyclin D1, Cyclin E, cyclin-dependent kinases (CDK1, CDK2, CDK4), and Ki67 protein—a marker of cell proliferation. Genes associated with cholesterol metabolism included sterol regulatory element-binding protein 2 (SREBP-2), acetyl-CoA cholesterol acyl-transferase (ACAT), 3-hydroxy-3-methylglutaryl-CoA reductase (HMGCR), mevalonate kinase (MVK), and mevalonate diphosphate decarboxylase (MVD). For lipid metabolism, genes such as acetyl-CoA carboxylase (ACC), ATP citrate lyase (ACLY), fatty acid synthase (FASN), acyl-CoA synthetase (ACS), and sterol regulatory element-binding protein 1 (SREBP-1) were included. Additionally, genes linked to glucose metabolism, such as glucose transporter 1 (GLUT1); genes related to hypoxia response factors, such as hypoxia-inducible factor 1α (HIF-1α); genes related to cell survival and anti-apoptosis, such as Survivin, cellular inhibitor of apoptosis protein 1 (cIAP1), and cIAP2; and genes related to epithelial-mesenchymal transition, such as N-Cadherin, Vimentin, Snail, and Twist were analyzed.

Biochemical assays were conducted on H520 tumor cells to study their metabolic characteristics, aiming to determine the drug's impact on cellular metabolism. Assessments included measuring lactate levels, lactate dehydrogenase (LDH) activation, ATP concentrations, and glucose uptake to evaluate glycolytic activity and overall energy metabolism. The inhibition rate was calculated using the formula: (Biochemical value of the control group - Biochemical value of the experimental group) / Biochemical value of the control group × 100%.[42,43] The findings were presented using a heatmap. The influence of HA-PTS@PCN on lipid metabolism in tumor tissues was further analyzed by[44,45] measuring the malondialdehyde (MDA) levels in subcutaneous tumor tissue lysates, following manufacturer's instructions and literature methods.

Statistical Analysis

The data are presented as mean ± standard error. Statistical significance for in vitro experiments was assessed using the *t*-test, while for in vivo experiments, one-way analysis of variance (ANOVA) was employed, followed by t-tests for multiple comparisons. A p-value of less than 0.05 was considered statistically significant.

Results

Synthesis and Characterization

In this study, we constructed a nanomaterial suitable for cellular uptake, PCN-224, based on TCPP using an in situ growth method. We subsequently loaded PTS molecules into PCN-224 to obtain PTS@PCN, which was then

encapsulated with HA to produce HA-PTS@PCN. The infrared (IR) spectra of the samples are shown in Figure 2A. Compared to PCN-224, PTS@PCN retained the characteristic peaks of PCN-224 at 1404 cm^{-1} and 1599 cm^{-1} after PTS loading; however, a distinct double peak appeared around 1000 cm^{-1}, attributed to the amino groups in PTS. Minimal changes in the IR spectra were observed before and after HA introduction, consistent with findings in other studies. The UV-vis absorption spectra of HA-PTS@PCN (Figure 2B) displayed the characteristic absorption peaks of TCPP, PCN-224, and HA-PTS@PCN. PCN-224 exhibited a strong absorption peak around 425 nm (Soret band) and four weaker peaks at 523 nm, 558 nm, 580 nm, and 640 nm, corresponding to the characteristic peaks of porphyrin materials. In the wavelength range of 300–800 nm, the UV absorption peaks of HA-PTS@PCN were significantly lower than those of TCPP and PCN-224, likely due to HA encapsulation, and the absorption peaks of PTS and HA did not appear within this range.

We conducted structural characterization of PCN-224, PTS@PCN, and HA-PTS@PCN using powder X-ray diffraction (PXRD) (Figure 2C). The diffraction peaks of the three samples were very similar, with distinct characteristic peaks at 4.49°, 6.44°, 7.86°, and 9.13°. These results indicate that both PTS@PCN and HA-PTS@PCN maintain the same framework structure as PCN-224, consistent with the literature values for PPCN-224. Additionally, the peaks of the NPs became less sharp after HA encapsulation. Scanning electron microscopy (SEM) was employed to observe the

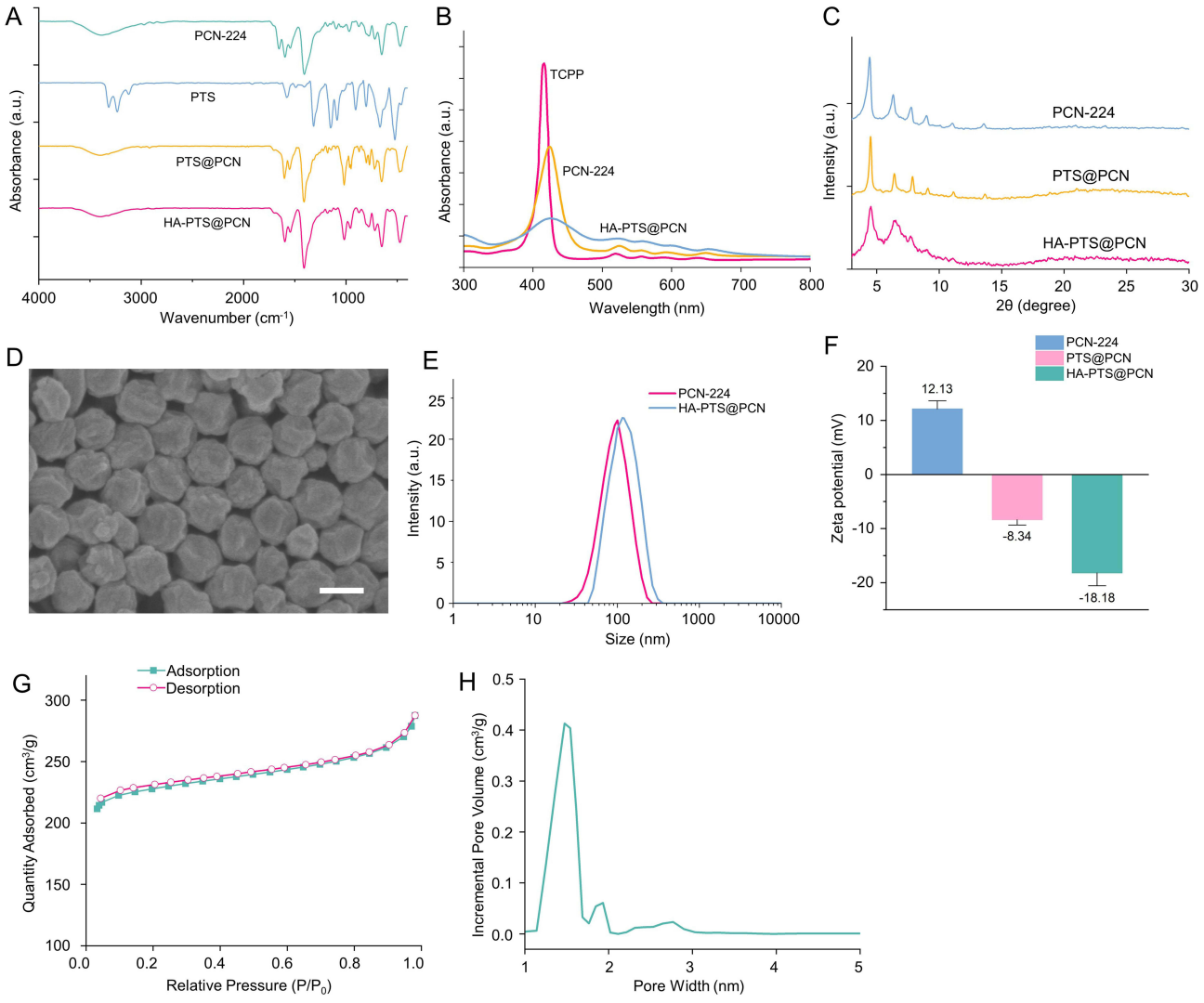

Figure 2 Structural characterization. (**A**) Infrared absorption spectrum; (**B**) UV-vis absorption spectrum; (**C**) PXRD spectrum; (**D**) Scanning electron microscopy images of HA-PTS@PCN, with a scale bar of 100 nm; (**E**) Particle size distribution; (**F**) Zeta potential; (**G**) N_2 adsorption-desorption isotherms of PCN-224; (**H**) Pore size distribution of HA-PTS@PCN.

https://doi.org/10.2147/DDDT.S504891

morphology of HA-PTS@PCN NPs (Figure 2D), revealing an irregular spherical structure with a uniform size of approximately 100 nm and excellent monodispersity. Dynamic light scattering (DLS) measurements (Figure 2E) indicated that the hydrated particle size of PCN-224 is 120.35 nm, which is larger than the size measured by SEM. DLS measures the particle size in solution, specifically the hydrated size, which includes both the nanoparticle core and the expanded micelle. Particles tend to swell in aqueous solutions, resulting in a hydrated size larger than that of dry particles. Zeta potential analysis (Figure 2F) revealed a significant change in surface charge from the positive potential of PCN-224 (+12.13 mV) to the negative potentials of PTS@PCN (−8.34 mV) and HA-PTS@PCN (−18.18 mV). PXRD and zeta potential data confirm the successful encapsulation of HA on the surface of the NPs. Nitrogen adsorption and desorption tests on PTS@PCN (Figure 2G) indicated a surface area of 683.25 m^2/g, which is smaller than that of PCN-224 (1852.82 m^2/g). This suggests that the incorporation of PTS into PCN-224 significantly affects the material's porosity. The pore structure characteristics of PCNs were analyzed using the Density Functional Theory model based on nitrogen adsorption isotherms. These materials exhibit highly uniform pores with pore sizes ranging from 1 nm to 2 nm (Figure 2H). Overall, these data confirm the successful preparation of HA-PTS@PCN.

In vitro ROS Generation

This study investigated the release of singlet oxygen ($^1O_2$) from various NPs under different in vitro conditions. Under conditions with only DPBF and normal light exposure, no $^1O_2$ was detected in the solvent, regardless of whether normal light or laser irradiation was used (Figure 3A). However, upon the addition of HA-PTS@PCN, significant $^1O_2$ release was observed under 660 nm laser irradiation, with the amount of release increasing over time. No significant $^1O_2$ release was observed in the HA-PTS@PCN group under normal light exposure. This indicates that HA-PTS@PCN significantly releases $^1O_2$ only under specific wavelength laser irradiation. Comparing the release capabilities of PCN-224, PTS@PCN, and HA-PTS@PCN, it was found that their $^1O_2$ release capabilities were similar (Figure 3B). Among them, PCN-224 exhibited the strongest release capability, closely followed by PTS@PCN, while the release capability of HA-PTS@PCN was slightly lower. However, as irradiation time increased, the differences between the two groups gradually diminished, possibly due to HA encapsulation delaying the release rate of $^1O_2$.

Subsequently, we examined the ROS generation capability of PCN-224, PTS@PCN, and HA-PTS@PCN in a cell-free environment using DCFH as a probe. Under 660 nm laser irradiation, the fluorescence intensity of DCFH increased over time (Figure 3C). In contrast, the ROS release rate from the HA-PTS@PCN group was significantly lower than that of the other two groups, likely due to HA encapsulation slowing ROS generation within the NPs. As irradiation time increased, the ROS release amounts from the three groups gradually converged, reaching similar levels at 10 minutes (Figure 3D). This experiment indicates that HA-PTS@PCN exhibits excellent ROS release capability in a cell-free environment.[46–48]

Acid-Responsive Degradation and Drug Release Process

PCN-224, as a drug loading platform, possesses characteristics of porosity and acid-responsive degradation. The coordination bonds between Zr and TCPP enable acid-responsive degradation in acidic environments. When preparing drug-loaded NPs, different concentrations of PTS and PCN-224 were mixed. The results showed that when the concentration ratio exceeded six times, the drug-loading capacity of PTS@PCN stabilized at approximately 138% (Figure 3E).

Due to the acidic microenvironment surrounding tumors, we investigated the drug release properties of HA-PTS @PCN in vitro under acidic conditions. HPLC was employed to determine the release of free PTS from the drug-loaded NPs. The experimental results (Figure 3F) indicated that, regardless of laser irradiation, the degradation rate of the NPs in phosphate-buffered saline (PBS) at pH 7.4 was relatively slow. During the first 6 hours, the release rate of HA-PTS @PCN was faster, but it gradually slowed thereafter. Under pH 5.5 conditions, the drug release from HA-PTS@PCN significantly increased, particularly with laser irradiation, where the release was notably faster than under the other three conditions. In the pH 5.5 + L group, drug release reached its maximum, approximately 82%, at 72 hours. Given the acidic tumor microenvironment, this material can selectively release a large amount of PTS within tumor cells.

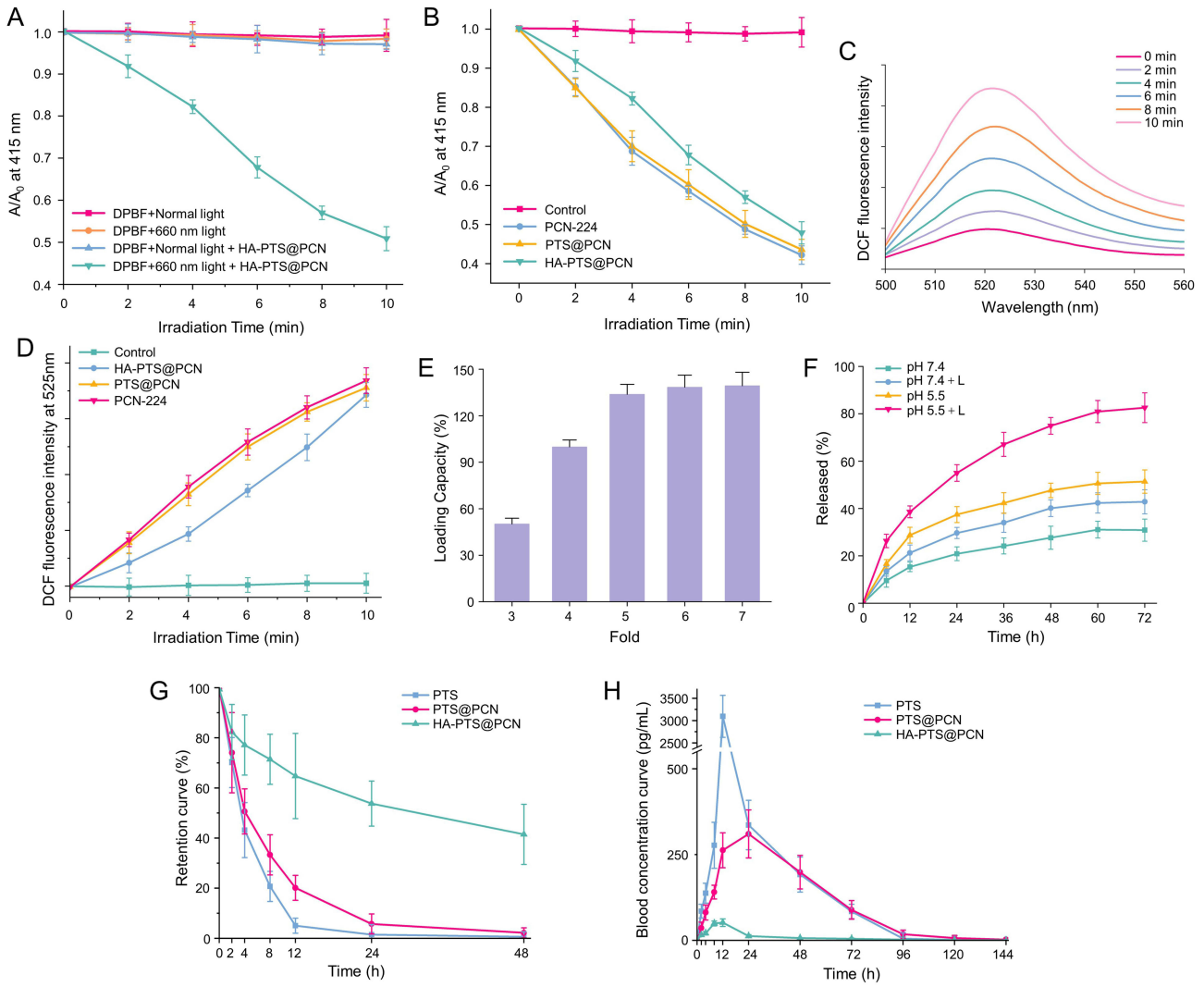

Figure 3 (**A**) $^1O_2$ release of NPs under 660 nm laser and ambient light irradiation, evaluated by DPBF consumption to assess $^1O_2$ generation; (**B**) $^1O_2$ release of different NPs under 660 nm laser irradiation; (**C**) Fluorescence absorption curves of NPs treated with DCFH-DA at 500–560 nm; (**D**) Fluorescence absorption values of different NPs at 525 nm; (**E**) Drug-loading capacity of HA-PTS@PCN at different PTS concentrations; (**F**) Drug release profile of HA-PTS@PCN under different pH conditions and laser irradiation; (**G**) Release profile of NPs in the tumor tissues of nude mice; (**H**) Blood concentration-time curve of NPs in nude mice.

Additionally, the thermal effect generated by laser irradiation can enhance this release. These experiments demonstrate that HA-PTS@PCN NPs exhibit acid-responsive drug release.

Changes in intratumoral PTS concentration at different time points after NP injection were detected using the LC-MS method. The results (Figure 3G) showed that when a PTS solution was directly injected into the tumor tissue, PTS was metabolized and cleared within 12 hours. However, when PTS@PCN was injected, the retention curve of PTS@PCN in the tumor tissue did not significantly differ from that of PTS. In comparison to direct PTS injection, HA-PTS@PCN achieved sustained release of PTS within the tumor tissue. After 48 hours, PTS content in the tumor tissue maintained approximately 40% of its peak value, indicating that only HA-PTS@PCN could achieve sustained release of PTS within the tumor.

Further examination of PTS concentration in the blood of tumor-bearing nude mice was conducted. The results (Figure 3H) showed that after injecting the PTS solution into the tumor tissue, the plasma concentration of PTS in the blood reached a peak of over 3000 pg/mL around 12 hours post-injection. Following this peak, the blood concentration of PTS declined rapidly, and by approximately 96 hours, PTS was almost completely metabolized and cleared from the mice, with levels dropping to near zero. The blood concentration curve for the PTS solution was essentially identical to

https://doi.org/10.2147/DDDT.S504891

that of PTS@PCN. In contrast, after injecting HA-PTS@PCN into the tumor, the PTS concentration in the blood of nude mice remained very low, returning to baseline by the 24-hour mark. These results indicated that HA-PTS@PCN had a prolonged retention time within the tumor and released minimal amounts into the bloodstream, suggesting excellent long-term sustained and controlled release properties.

Intracellular ROS Release

After treating H520 cells with different NPs (including the Control group, PCN-224+L group, PTS@PCN+L group, and HA-PTS@PCN+L group) for various durations (0, 4, 8, 12, and 24 hours) followed by laser irradiation, the ROS content in the cells was measured. The results (Figure 4A and B) showed that at around 4 hours, ROS levels were similar across all groups and remained low, primarily because the NPs had not yet significantly entered the cells at this stage. From the 8-hour mark onward, ROS release levels increased substantially, indicating that cellular uptake of NPs peaked before and after this time. At approximately 12 hours, the ROS release levels in the PCN-224+L and PTS@PCN+L groups were similar, but the PTS@PCN+L group gradually surpassed the PCN-224+L group. At the 24-hour time point, the order of ROS release strength from the NPs was HA-PTS@PCN > PTS@PCN > PCN-224. This result was consistent with the 24-hour cellular uptake findings, suggesting that HA-PTS@PCN exhibited high efficiency in ROS generation, prolonged retention time, and sustained ROS production, making it less likely to be cleared by tumor cells. This may be attributed to PTS inhibiting the expression of certain proteins in the cells (such as GPX4), thereby reducing the rate of ROS clearance. The HA-PTS@PCN+L group exhibited the strongest ROS release capability, primarily due to the HA coating, which enhanced nanoparticle uptake and delayed the structural breakdown of PCN-224, thus extending the duration of ROS release.[33–36]

Cellular Uptake

The cellular uptake experiment investigated the content of NPs in cell lysates using the HPLC method. The results (Figure 4C) demonstrated that within the first 6 hours of co-incubation with PTS or HA-PTS@PCN, the uptake of both was approximately the same (calculated by PTS content). However, after 24 hours, the cellular uptake of HA-PTS@PCN reached approximately 9%, significantly higher than that of the PTS group. Compared to direct PTS administration, loading PTS and encapsulating it within HA in PCN-224 NPs enhanced the transport of PTS into the cells, thereby increasing intracellular drug concentration and retention.

Cytotoxicity

The cytotoxicity of PTS, PCN-224, PTS@PCN, HA@PCN, and HA-PTS@PCN was assessed using the MTT assay. The results (Figure 4D) showed that the 660 nm laser alone (Control group) had negligible effects on cell viability, indicating minimal phototoxicity from light exposure in H520 cells. Both PTS and PCN-224 exhibited moderate inhibitory effects under laser irradiation. The cytotoxicity was significantly enhanced when PTS was combined with PCN-224, and further intensified with increasing concentrations of PTS@PCN. Notably, HA-PTS@PCN demonstrated significantly higher cytotoxicity at all concentrations compared to the PTS@PCN group, suggesting a superior anti-tumor effect. This indicates that HA encapsulation can enhance the inhibitory effect of NPs on tumor cells. Additionally, comparing the PCN-224 group with the PTS@PCN group (Figure 4D), and the HA@PCN group with the HA-PTS@PCN group (Figure S1), it was found that NPs containing PTS consistently exhibited significantly higher cytotoxicity. This underscores the indispensability of PTS loading for enhancing the cytotoxicity of NPs.

To further assess the impact of HA-PTS@PCN NPs on cell viability, a plate cloning assay was used to examine the cytotoxic effects on H520 cells (Figure 4E and F). The assay showed that 20 μg/mL of PTS minimally inhibited cell growth. The PCN-224 group also showed limited inhibition, slightly better than the PTS group. However, the PTS@PCN group demonstrated a more substantial inhibitory capacity, indicating that PTS enhances the phototherapy capabilities of PCN-224. HA-PTS@PCN showed the most optimal inhibitory effect, consistent with predictions. The experiment confirmed that laser irradiation significantly enhanced the inhibitory effect of HA-PTS@PCN NPs on H520 cells, and irrespective of the presence or absence of laser irradiation, the inhibitory capacity of the NPs on cell growth was

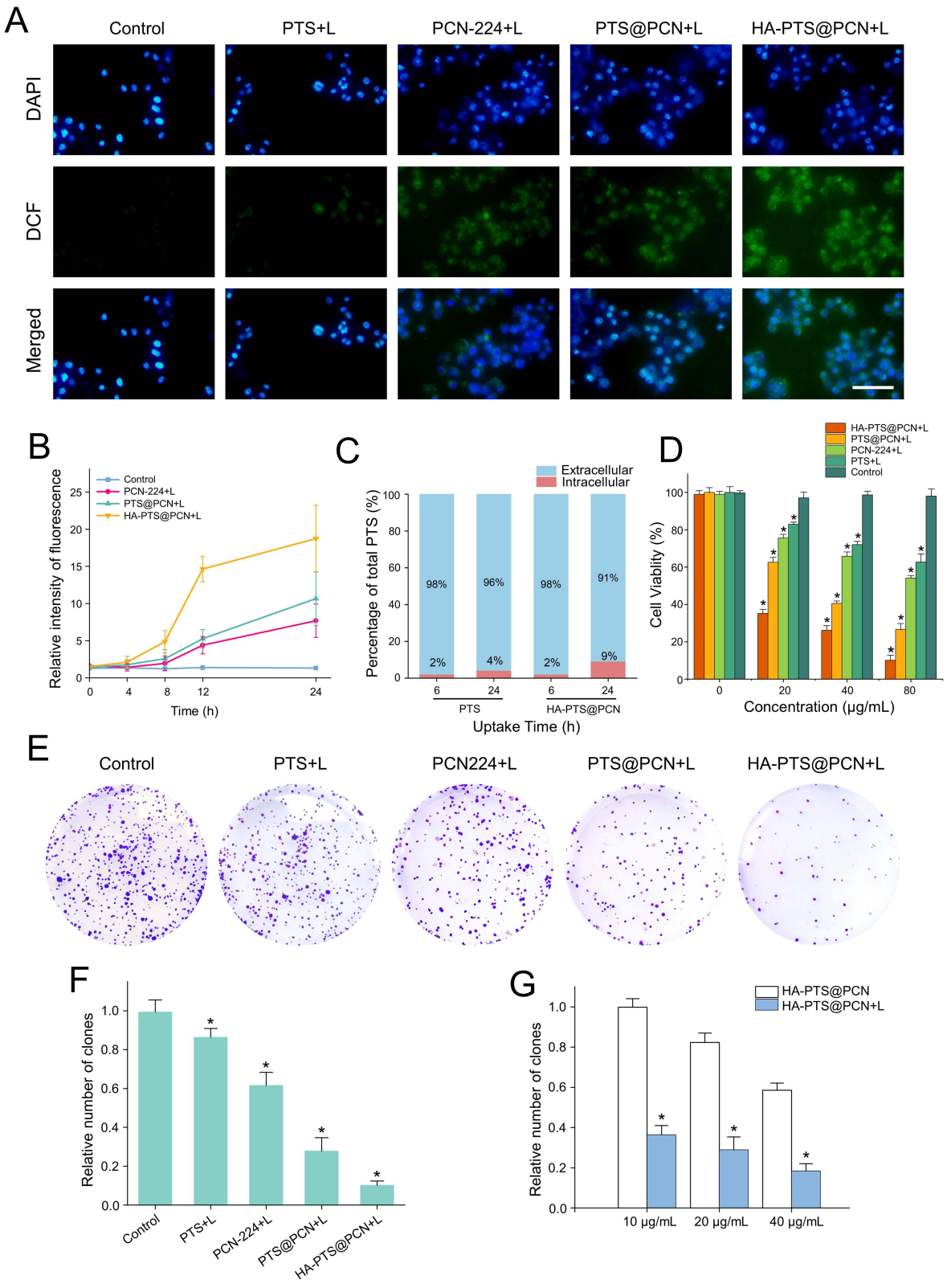

Figure 4 (**A**) Using DCFH as an intracellular ROS probe, the ROS release was detected after co-incubation of different NPs with H520 cells for 12 hours under 660 nm laser irradiation, scale bar is 50 μm; (**B**) Quantitative analysis of ROS release after co-incubation of different NPs with H520 cells for different times; (**C**) Cellular uptake of PTS or HA-PTS@PCN by H520 cells after different co-incubation times (measured as PTS); (**D**) Cytotoxicity of different concentrations of NPs (measured as PTS) on H520 cells after 660 nm laser irradiation (n = 8/group); (**E**) Plate cloning assay of different NPs; (**F**) Quantitative analysis of the plate cloning assay of different NPs (n = 6/group); (**G**) Quantitative analysis of the cell cloning experiment with different concentrations of HA-PTS@PCN under laser irradiation and without laser irradiation (n = 6/group). Data are expressed as the mean ± SD (n = 6 or more independent biological replicates); *P<0.05.

https://doi.org/10.2147/DDDT.S504891

positively correlated with their administered concentration (Figure 4G). The plate cloning assay confirmed the significant cytotoxic effects of HA-PTS@PCN on H520 cells.

To explore the antitumor mechanisms of the NPs, live/dead cell staining and flow cytometry assays were conducted (Figure 5A and B, with green and red fluorescence indicating live and dead cells, respectively). Results indicated a low number of dead cells in the Control group, PTS+L group, and PCN-224+L group. The number of dead cells significantly increased in the PTS@PCN+L group and was highest in the HA-PTS@PCN+L group, approaching 100%. This demonstrates the strong antitumor effects of the synergistic action between PTS and PDT.

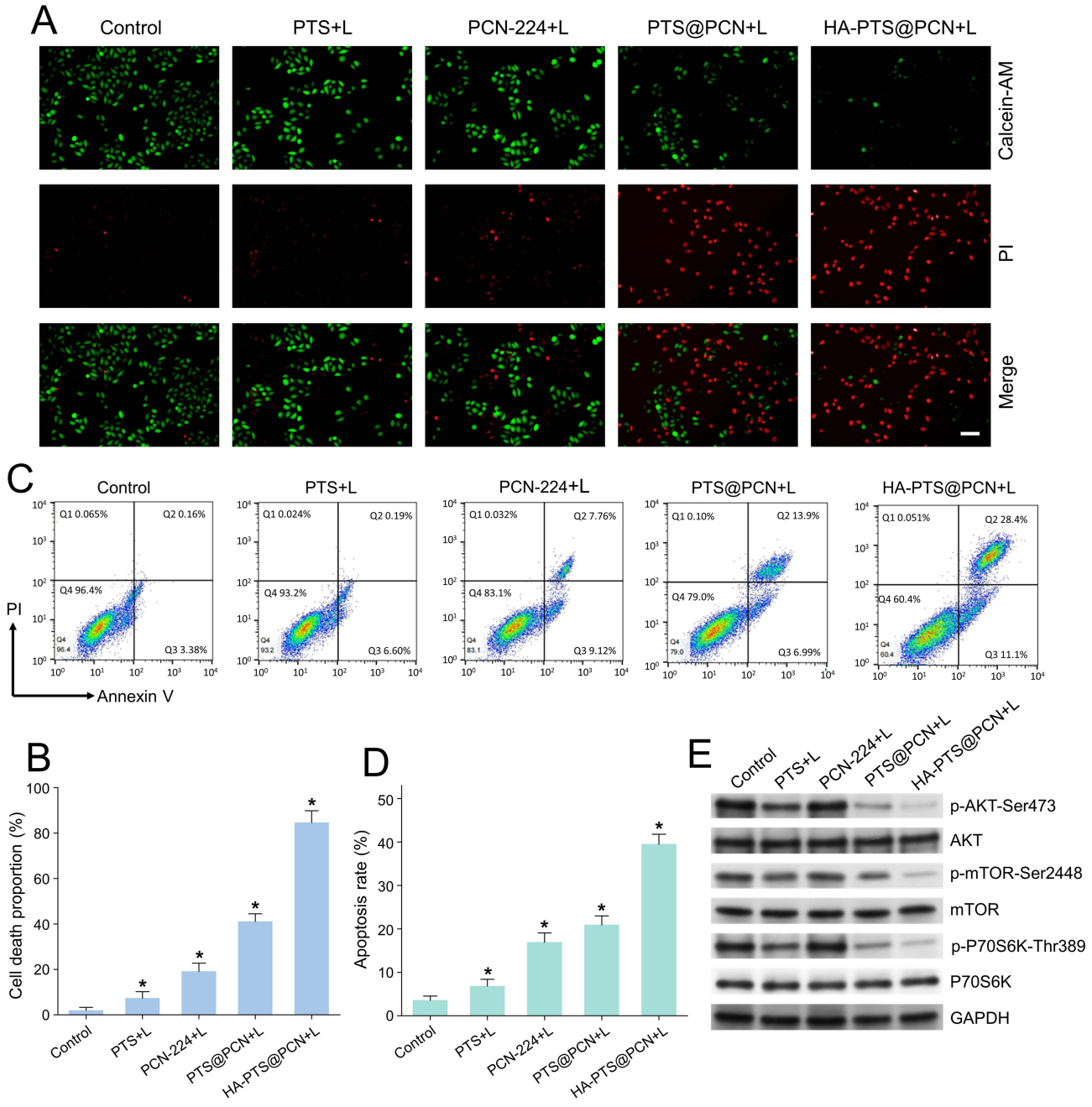

Figure 5 (**A**) Live/dead cell staining images of H520 cells treated with different NPs. Green fluorescence: live cells, red fluorescence: dead cells. Scale bar is 50 μm; (**B**) Quantitative statistics of dead cell staining in H520 cells treated with different NPs (n = 6/group); (**C**) Flow cytometry analysis of apoptosis in H520 cells treated with different samples using Annexin V/PI staining; (**D**) Quantitative results of flow cytometry analysis, with cells in Q2 and Q3 considered as apoptotic cells (n = 6/group); (**E**) Western blot analysis of protein expression levels after treatment with different NPs. Data are expressed as the mean ± SD (n = 6 or more independent biological replicates); *P<0.05.

 https://doi.org/10.2147/DDDT.S504891

Flow cytometry was also used to quantify cell stages post-treatment (Figure 5C and D). Twenty-four hours after PTS treatment, early apoptotic cells (Annexin V+/PI−) significantly increased. The proportions of late apoptotic/necrotic cells (Annexin V+/PI+) were 0.19%, 7.76%, 13.9%, and 28.4% in the PTS, PCN-224+L, PTS@PCN+L, and HA-PTS@PCN +L groups, respectively. These results indicate that HA-PTS@PCN induces apoptosis in tumor cells.

Expression of Related Factors After PTS Treatment

To elucidate the molecular mechanism by which HA-PTS@PCN promotes apoptosis, Western blot analysis was used to detect changes in protein expression related to the AKT-mTOR pathway (Figure 5E). PTS only slightly inhibited the protein expression of the PI3K/AKT signaling pathway (p-AKT-Ser473, p-mTOR-Ser2448, and p-P70S6K-Thr389) without affecting the levels of AKT, mTOR, and P70S6K proteins. The PCN-224+L group did not affect these protein' expression. However, HA-PTS@PCN+L significantly inhibited the expression of proteins associated with the PI3K/AKT signaling pathway (p-AKT-Ser473, p-mTOR-Ser2448, and p-P70S6K-Thr389) without affecting the expression levels of AKT, mTOR, and P70S6K total protein, suggesting a more potent effect. Interestingly, the inhibitory capacity of PTS@PCN+L was slightly lower than that of HA-PTS@PCN+L. These results demonstrated that loading PTS into PCN-224 offers a sustained release effect, enhancing the drug's retention time in cells and increasing the inhibition of PTS. Additionally, HA encapsulation increases cellular uptake of the NPs, further enhancing their inhibitory effect.

In vivo Antitumor Activity

The experimental data were primarily obtained from in vitro tests. To further confirm the antitumor activity of HA-PTS @PCN, this study constructed a subcutaneous tumor model in nude mice and conducted an in vivo pharmacodynamic evaluation. PTS@PCN and HA-PTS@PCN were injected into the subcutaneous tumor tissues of nude mice, followed by laser irradiation. The results (Figure 6A and B) showed that the injection of HA-PTS@PCN into the tumor tissues exhibited significant antitumor activity. In contrast, the injection of PTS@PCN did not demonstrate substantial antitumor effects. Following the injection of HA-PTS@PCN and subsequent laser irradiation, tumor growth was significantly inhibited, and the rate of tumor volume increase slowed. Notably, the injection of PTS@PCN with laser irradiation also displayed some antitumor activity, indicating that the photodynamic effect enhanced the antitumor capabilities of PTS@PCN. The tumor weight and body weight data of the mice are presented in the supplementary file (Table S1).

To elucidate the mechanisms by which HA-PTS@PCN and PTS@PCN affect tumor growth, this study examined the gene expression of various metabolism-related factors in the tumor tissues of nude mice before and after treatment. The experimental results (Figure 6C) indicated that intratumoral injection of PTS@PCN only slightly reduced the expression of cholesterol synthesis-related factors (SREBP-2, ACAT, HMGCR, MVK, and MVD), pro-survival factors, and epithelial-mesenchymal transition (EMT) factors (Survivin, cIAP-1, cIAP-2, Vimentin, N-Cadherin, Twist, and Snail), as well as some cell proliferation-related factors (Cyclin D1, Cyclin E, Cyclin B, CDK1, CDK2, CDK4, and Ki67). Phototherapy further enhanced the effects of PTS@PCN. Regardless of phototherapy, intratumoral injection of HA-PTS @PCN did not affect the expression of fatty acid anabolism-related factors (including SREBP-1, ACC, ACLY, FASN, and ACS), but it significantly reduced the expression of cholesterol synthesis-related factors (SREBP-2, ACAT, HMGCR, MVK, and MVD), pro-survival factors, EMT factors (Survivin, cIAP-1, cIAP-2, Vimentin, N-Cadherin, Twist, and Snail), and cell proliferation-related factors (Cyclin D1, Cyclin E, Cyclin B, CDK1, CDK2, CDK4, and ki67).

Further examination of the metabolic characteristics in tumor tissues after different treatments revealed that, as shown in Figure 6D, the levels of lactate, LDH activation, ATP, and glucose uptake in the tumor tissues were significantly inhibited following HA-PTS@PCN photodynamic therapy. The MDA level associated with the induction of ferroptosis was upregulated. Moreover, after photodynamic therapy, these effects were more pronounced, whereas PTS@PCN alone had only minimal impact. These experiments demonstrated that HA-PTS@PCN photodynamic therapy inhibited tumor tissue growth through two molecular mechanisms: by suppressing the gene expression of cell proliferation-related factors and by inhibiting the gene expression of metabolism-related factors within the tumor tissue.

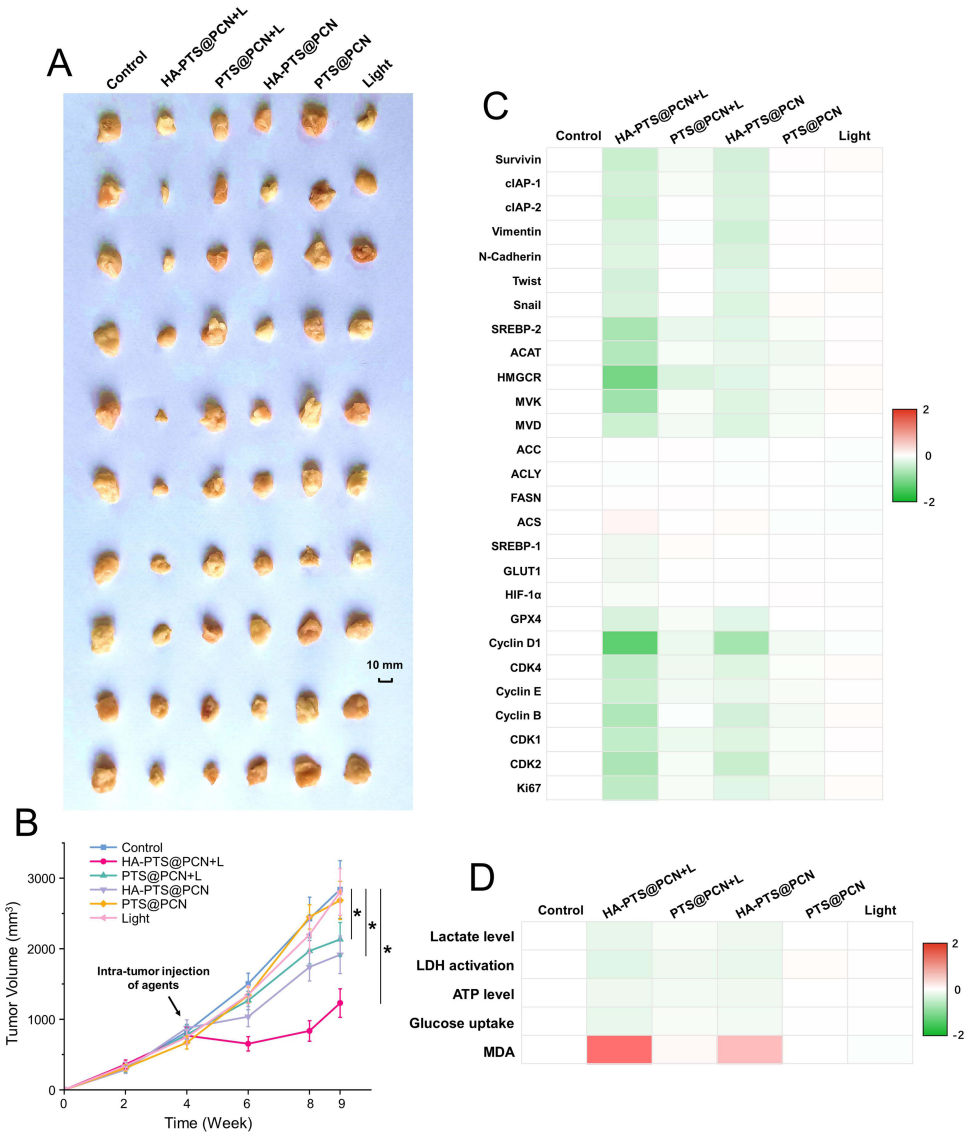

Figure 6 In vivo antitumor activity of different NPs on H520 tumors. (**A**) Photographs of tumor tissues; (**B**) Tumor volume change curves (n = 10/group); (**C**) Expression levels of various metabolism-related factors in tumor tissues after treatment; (**D**) Changes in metabolic characteristics in tumor tissues after treatment. Data are expressed as the mean ± SD (n = 6 or more independent biological replicates); *P<0.05.

Discussion

PDT has emerged as a promising modality for tumor treatment, characterized by its minimal invasiveness, low toxicity, and high selectivity. These attributes have positioned PDT as a viable option for the clinical management of various superficial tumors, demonstrating broad application prospects. However, in practical applications, the limited tissue penetration of laser light has been identified as a significant constraint. This limitation restricts the efficacy of PDT in treating deep-seated tumors, rendering it more effective only for superficial lesions. Moreover, while increasing laser power and prolonging exposure time may enhance therapeutic outcomes to some extent, these approaches are associated with the risk of adverse effects, such as skin burns, which in turn restrict the further clinical application of PDT.

In light of these challenges, the present study explores the introduction of PTS as a sensitizer to enhance the sensitivity of tumors to PDT, thereby improving overall therapeutic efficacy. The strategy of employing sensitizers to augment tumor sensitivity to therapeutic modalities has been widely applied in chemotherapy and radiotherapy, yielding satisfactory results. However, to date, no reports have documented the application of sensitizers in PDT. Therefore, the

initiation of this study is anticipated to not only break through the bottleneck of PDT in treating deep-seated tumors but also provide new insights and directions for optimizing PDT, holding significant scientific and clinical value.

The HA-PTS@PCN NPs developed in this study have been thoroughly characterized using various structural characterization techniques, confirming the accuracy and rationality of their design. These nanoparticles exhibit high drug loading capacity for PTS and demonstrate excellent stability in both neutral and weakly acidic environments, enabling efficient drug release. Notably, the drug release capacity of HA-PTS@PCN NPs is significantly enhanced in weakly acidic conditions compared to neutral conditions, making them highly suitable for targeted drug release in the acidic microenvironment of tumor tissues. In vivo and in vitro drug release experiments revealed that HA-PTS@PCN NPs can slowly and sustainably release PTS into tumor tissues, effectively maintaining the drug concentration of PTS in the body. This release rate is significantly lower than that of directly administered PTS. The sustained-release characteristic of HA-PTS @PCN NPs allows them to achieve strong tumor-sensitizing effects even with a low dose of PTS, which is markedly superior to the traditional administration of PTS alone. In the ROS release experiment, the HA-PTS@PCN group exhibited the highest ROS release capacity. This result is primarily attributed to the HA coating, which significantly enhanced the cellular uptake of NPs, thereby increasing the intracellular content of NPs. Additionally, the HA coating delayed the structural degradation of PCN-224, thereby prolonging the release time of ROS. The combination of high activity and sustained-release properties endows HA-PTS@PCN with greater potential for pharmaceutical applications compared to PTS@PCN.Cell uptake experiments compared the differences between PTS administered alone and PTS formulated as NPs. The results indicated that formulating PTS into NPs significantly enhanced cellular uptake of PTS, thereby greatly improving the utilization efficiency of PTS by cells. This experiment further confirmed the importance of nanoencapsulation for PTS, which is crucial for efficiently exerting the tumor-sensitizing function of PTS. Moreover, this study evaluated the cytotoxicity of various samples using two different experimental methods: MTT assays and colony formation assays. Both experiments showed that while the cytotoxicity of the HA@PCN group was higher than that of the PCN-224 group, it was significantly lower than that of the HA-PTS@PCN group. This indicates that the loading of PTS is essential for enhancing the cytotoxicity of NPs, further highlighting the critical role of PTS in the nanomedicine system.

The PI3K/AKT signaling pathway plays a crucial role in cell cycle regulation, and its inhibition can lead to cell cycle arrest, rendering cells more susceptible to various external stimuli. Results from Western blot experiments demonstrated that HA-PTS@PCN significantly suppressed the expression of key proteins in the PI3K/AKT signaling pathway, including p-AKT-Ser473, p-mTOR-Ser2448, and p-P70S6K-Thr389. This inhibitory effect was more pronounced than that achieved by direct administration of PTS. These mechanistic findings are highly consistent with the pharmacodynamic data obtained from both in vitro and in vivo experiments, further confirming that HA-PTS@PCN exerts its PDT sensitization effect through the inhibition of the PI3K/AKT signaling pathway. Comprehensive analysis of the gene expression of various proliferation- and metabolism-related factors in tumor tissues from nude mice before and after treatment revealed that HA-PTS@PCN significantly downregulated the expression of factors involved in cholesterol synthesis, pro-survival factors, EMT-related factors, and cell proliferation-related factors. These results indicate that HA-PTS@PCN exerts its anti-tumor effects through multi-target inhibition, providing strong evidence to elucidate its underlying mechanism of action.

In this study, the combination of PDT with a drug-sensitization strategy significantly enhanced the therapeutic efficacy of PDT against lung cancer. This multi-target synergistic mechanism not only provides a novel approach for the treatment of lung cancer but also paves the way for the treatment of other types of tumors. Compared with previously reported MOFs - based PDT drugs, the drug developed in this study is capable of more effectively harnessing the therapeutic potential of PDT. Its unique design and mechanism of action endow it with broader clinical application prospects and can be promoted as an innovative therapeutic strategy for the development and application of other PDT drugs, offering important reference value for improving the overall efficacy of PDT.

Conclusion

In summary, we have developed a PDT nanodrug delivery platform based on porphyrin MOFs. This platform loads PTS into PCN-224 and is externally wrapped with HA to enhance cellular uptake. The material effectively leverages the porous structure and photodynamic properties of PCN-224, as well as the tumor-sensitizing effects of PTS. By slowly releasing PTS, the material increases the sensitivity of tumor tissues to phototherapy, thereby improving the therapeutic

efficacy of PDT. Additionally, it selectively releases in the mildly acidic environment of tumors. Both in vitro and in vivo experimental results indicate that the combined photothermal and sensitization therapy exhibits excellent therapeutic effects on lung cancer. The properties of HA-PTS@PCN NPs enhance the sensitivity of tumor tissues to PDT, enabling effective therapeutic outcomes with low-dose laser irradiation and thereby improving patient tolerability.

This study also elucidated the pharmacokinetic mechanisms of HA-PTS@PCN NPs and the antitumor molecular mechanisms at the in vivo, cellular, and molecular levels. In conclusion, HA-PTS@PCN NPs possess high drug-loading capacity, excellent phototherapeutic effects, and selective release capabilities, making them a promising platform for synergistic cancer therapy.

Author Contributions

All authors made a significant contribution to the work reported, whether that is in the conception, study design, execution, acquisition of data, analysis and interpretation, or in all these areas; took part in drafting, revising or critically reviewing the article; gave final approval of the version to be published; have agreed on the journal to which the article has been submitted; and agree to be accountable for all aspects of the work.

Funding

The authors gratefully acknowledge financial support from the program for the National High Level Hospital Clinical Research Funding (Grant No. BJ-2022-107).

Disclosure

The authors declare that they have no conflicts of interest in this work.

References

1. Falzone L, Salomone S, Libra M. Evolution of cancer pharmacological treatments at the turn of the third millennium. *Front Pharmacol*. 2018;9:1300. doi:10.3389/fphar.2018.01300
2. Lv D, Xu C, Wang C, Sang Q. Lung squamous cell carcinoma with EML4-ALK fusion and TP53 co-mutation treated with ensartinib: a case report and literature review. *Chinese J Lung Cancer*. 2023;26(1):78–82. doi:10.3779/j.issn.1009-3419.2023.106.03
3. Jiang W, Zhou Y, Zeng L, et al. The efficacy and safety of albumin-bound paclitaxel plus carboplatin as neoadjuvant therapy for potentially resectable lung squamous cell carcinoma: a real-world retrospective cohort study. *Transl Lung Cancer Res*. 2022;11(4):647–655. doi:10.21037/tlcr-22-252
4. Dong M, Liu J, Gong H, et al. The analysis of surgical prognostic factors and molecular typing of locally advanced lung squamous cell carcinomas. *Asia-Pac J Clini Oncol*. 2021;17(5):e226–e237. doi:10.1111/ajco.13438
5. Kim TE, Chang JE. Recent studies in photodynamic therapy for cancer treatment: from basic research to clinical trials. *Pharmaceutics*. 2023;15(9):2257. doi:10.3390/pharmaceutics15092257
6. Zhao M, Hao D, Wu Q, et al. Porphyrin cholesterol conjugates for enhanced photodynamic immunotherapy toward lung cancer. *ACS Appl Mater Interfaces*. 2023;15(30):35927–35938. doi:10.1021/acsami.3c05825
7. Sun W, Zhang Q, Wang X, Jin Z, Cheng Y, Wang G. Clinical practice of photodynamic therapy for non-small cell lung cancer in different scenarios: who is the better candidate? *Respiration Int Rev Thoracic Dis*. 2024;103(4):193–204. doi:10.1159/000535270
8. Zhang P, Zheng L, Zhang X, et al. Mesoporous graphene oxide nanocomposite effective for combined chemo/photo therapy against non-small cell lung cancer. *Int j Nanomed*. 2024;19:7493–7508. doi:10.2147/IJN.S460767
9. Chen L, Ye X, Hu K, et al. Population pharmacokinetic modeling and simulation of HPPH in Chinese patients with esophageal carcinoma. *Xenobiotica*. 2020;50(2):170–177. doi:10.1080/00498254.2019.1597315
10. Anand S, Hasan T, Maytin EV. Treatment of nonmelanoma skin cancer with pro-differentiation agents and photodynamic therapy: preclinical and clinical studies (Review). *Photochemistr Photobiol*. 2024;100(6):1541–1560. doi:10.1111/php.13914
11. Sun X, He G, Xiong C, et al. One-pot fabrication of hollow porphyrinic MOF nanoparticles with ultrahigh drug loading toward controlled delivery and synergistic cancer therapy. *ACS Appl Mater Interfaces*. 2021;13(3):3679–3693. doi:10.1021/acsami.0c20617
12. Li X, Qin H, Zhou Z, et al. Cellular evaluation of the metal-organic framework PCN-224 associated with inflammation and autophagy. *Toxicol in vitro*. 2021;70:105019. doi:10.1016/j.tiv.2020.105019
13. Zhang Y, Wang Q, Chen G, Shi P. DNA-functionalized metal-organic framework: cell imaging, targeting drug delivery and photodynamic therapy. *Inorganic Chemistry*. 2019;58(10):6593–6596. doi:10.1021/acs.inorgchem.9b00734
14. Correia JH, Rodrigues JA, Pimenta S, Dong T, Yang Z. Photodynamic therapy review: principles, photosensitizers, applications, and future directions. *Pharmaceutics*. 2021;13(9):1332. doi:10.3390/pharmaceutics13091332
15. Ji B, Wei M, Yang B. Recent advances in nanomedicines for photodynamic therapy (PDT)-driven cancer immunotherapy. *Theranostics*. 2022;12(1):434–458. doi:10.7150/thno.67300
16. Overchuk M, Weersink RA, Wilson BC, Zheng G. Photodynamic and photothermal therapies: synergy opportunities for nanomedicine. *ACS nano*. 2023;17(9):7979–8003. doi:10.1021/acsnano.3c00891
17. Feng Y, Jiang Q, Ma X, et al. Photosensitizing metal-organic framework nanoparticles combined with tumor-sensitization strategies can enhance the phototherapeutic effect upon medullary thyroid carcinoma. *Biochim Biophys Acta Gen Subj*. 2024;1868(12):130725. doi:10.1016/j.bbagen.2024.130725

18. Shen C, Shyu DL, Xu M, et al. Deregulation of AKT-mTOR signaling contributes to chemoradiation resistance in lung squamous cell carcinoma. *mol Cancer Res*. 2022;20(3):425–433. doi:10.1158/1541-7786.MCR-21-0272
19. Huang S, Du K, Liu Z, Li J. Inhibition of mTOR by temsirolimus overcomes radio-resistance in nasopharyngeal carcinoma. *Clin Exp Pharmacol Physiol*. 2022;49(7):703–709. doi:10.1111/1440-1681.13649
20. Niu Y, Zeng X, Qin G, Zhang D, Zhou J, Chen L. Downregulation of metabotropic glutamate receptor 5 alleviates central sensitization by activating autophagy via inhibiting mTOR pathway in a rat model of chronic migraine. *Neurosci lett*. 2021;743:135552. doi:10.1016/j.neulet.2020.135552
21. Beck JT, Ismail A, Tolomeo C. Targeting the phosphatidylinositol 3-kinase (PI3K)/AKT/mammalian target of rapamycin (mTOR) pathway: an emerging treatment strategy for squamous cell lung carcinoma. *Cancer Treat Rev*. 2014;40(8):980–989. doi:10.1016/j.ctrv.2014.06.006
22. Hsu JL, Leu WJ, Zhong NS, Guh JH. Autophagic activation and decrease of plasma membrane cholesterol contribute to anticancer activities in non-small cell lung cancer. *Molecules*. 2021;26(19):5967. doi:10.3390/molecules26195967
23. Hsu JL, Leu WJ, Hsu LC, Liu SP, Zhong NS, Guh JH. Para-toluenesulfonamide induces anti-tumor activity through Akt-dependent and -independent mTOR/p70S6K pathway: roles of lipid raft and cholesterol contents. *Front Pharmacol*. 2018;9:1223. doi:10.3389/fphar.2018.01223
24. He J, Ying W, Yang H, et al. Gemcitabine plus cisplatin chemotherapy with concurrent para-toluenesulfonamide local injection therapy for peripherally advanced nonsmall cell lung cancer larger than 3 cm in the greatest dimension. *Anti-Cancer Drugs*. 2009;20(9):838–844. doi:10.1097/CAD.0b013e32832fe48f
25. Li SY, Li Q, Guan WJ, et al. Effects of para-toluenesulfonamide intratumoral injection on non-small cell lung carcinoma with severe central airway obstruction: a multi-center, non-randomized, single-arm, open-label trial. *Lung Cancer*. 2016;98:43–50. doi:10.1016/j.lungcan.2016.05.012
26. Guan WJ, Li SY, Zhong NS. Effects of para-toluenesulfonamide intratumoral injection on pulmonary adenoid cystic carcinoma complicating with severe central airway obstruction: a 5-year follow-up study. *J Thoracic Dis*. 2018;10(4):2448–2455. doi:10.21037/jtd.2018.03.70
27. Park J, Jiang Q, Feng D, Mao L, Zhou HC. Size-controlled synthesis of porphyrinic metal-organic framework and functionalization for targeted photodynamic therapy. *J Am Chem Soc*. 2016;138(10):3518–3525. doi:10.1021/jacs.6b00007
28. Wang J, Fan Y, Tan Y, et al. Porphyrinic metal-organic framework PCN-224 nanoparticles for near-infrared-induced attenuation of aggregation and neurotoxicity of alzheimer's amyloid-β peptide. *ACS Appl Mater Interfaces*. 2018;10(43):36615–36621. doi:10.1021/acsami.8b15452
29. Zeng R, He T, Lu L, Li K, Luo Z, Cai K. Ultra-thin metal-organic framework nanosheets for chemo-photodynamic synergistic therapy. *J Mat Chem B*. 2021;9(20):4143–4153. doi:10.1039/D1TB00528F
30. Yao X, Chen D, Zhao B, et al. Acid-degradable hydrogen-generating metal-organic framework for overcoming cancer resistance/metastasis and off-target side effects. *Adv Sci*. 2022;9(10):e2101965. doi:10.1002/advs.202101965
31. Xie BR, Yu Y, Liu XH, et al. A near infrared ratiometric platform based π-extended porphyrin metal-organic framework for O(2) imaging and cancer therapy. *Biomaterials*. 2021;272:120782. doi:10.1016/j.biomaterials.2021.120782
32. Tehrani Nejad S, Rahimi R, Najafi M, Rostamnia S. Sustainable gold nanoparticle (Au-NP) growth within interspaces of porphyrinic zirconium-based metal-organic frameworks: green synthesis of PCN-224/Au-NPs and its anticancer effect on colorectal cancer cells assay. *ACS Appl Mater Interfaces*. 2024;16(3):3162–3170. doi:10.1021/acsami.3c15398
33. Han D, Jiang L, Gu X, et al. SIRT3 deficiency is resistant to autophagy-dependent ferroptosis by inhibiting the AMPK/mTOR pathway and promoting GPX4 levels. *J Cell Physiol*. 2020;235(11):8839–8851. doi:10.1002/jcp.29727
34. Sun Y, Berleth N, Wu W, et al. Fin56-induced ferroptosis is supported by autophagy-mediated GPX4 degradation and functions synergistically with mTOR inhibition to kill bladder cancer cells. *Cell Death Dis*. 2021;12(11):1028. doi:10.1038/s41419-021-04306-2
35. Sui X, Zhang R, Liu S, et al. RSL3 drives ferroptosis through GPX4 inactivation and ROS production in colorectal cancer. *Front Pharmacol*. 2018;9:1371. doi:10.3389/fphar.2018.01371
36. Wang X, Shen T, Lian J, et al. Resveratrol reduces ROS-induced ferroptosis by activating SIRT3 and compensating the GSH/GPX4 pathway. *Mol Med*. 2023;29(1):137. doi:10.1186/s10020-023-00730-6
37. Jiang Q, Zhang M, Sun Q, Yin D, Xuan Z, Yang Y. Enhancing the antitumor effect of doxorubicin with photosensitive metal-organic framework nanoparticles against breast cancer. *Mol Pharmaceut*. 2021;18(8):3026–3036. doi:10.1021/acs.molpharmaceut.1c00249
38. Cheki M, Mostafaei S, Hanafi MG, et al. Radioproteomics modeling of metformin-enhanced radiosensitivity: an animal study. *Japanese J Radiol*. 2023;41(11):1265–1274. doi:10.1007/s11604-023-01445-8
39. Guerrero M, Ferrín G, Rodríguez-Perálvarez M, et al. mTOR expression in liver transplant candidates with hepatocellular carcinoma: impact on histological features and tumour recurrence. *Int J mol Sci*. 2019;20(2):336–351. doi:10.3390/ijms20020336
40. Song W, Tweed JA, Visswanathan R, Saunders JP, Gu Z, Holliman CL. Bioanalysis of targeted nanoparticles in monkey plasma via LC-MS/MS. *Anal Chem*. 2019;91(21):13874–13882. doi:10.1021/acs.analchem.9b03367
41. Li P, Lin Q, Sun S, et al. Inhibition of cannabinoid receptor type 1 sensitizes triple-negative breast cancer cells to ferroptosis via regulating fatty acid metabolism. *Cell Death Dis*. 2022;13(9):808. doi:10.1038/s41419-022-05242-5
42. Zhou W, Gao Y, Tong Y, Wu Q, Zhou Y, Li Y. Anlotinib enhances the antitumor activity of radiofrequency ablation on lung squamous cell carcinoma. *Pharmacol Res*. 2021;164:105392. doi:10.1016/j.phrs.2020.105392
43. Wang JH, Zeng Z, Sun J, Chen Y, Gao X. A novel small-molecule antagonist enhances the sensitivity of osteosarcoma to cabozantinib in vitro and in vivo by targeting DNMT-1 correlated with disease severity in human patients. *Pharmacol Res*. 2021;173:105869. doi:10.1016/j.phrs.2021.105869
44. Yin F, Feng F, Wang L, Wang X, Li Z, Cao Y. SREBP-1 inhibitor Betulin enhances the antitumor effect of Sorafenib on hepatocellular carcinoma via restricting cellular glycolytic activity. *Cell Death Dis*. 2019;10(9):672. doi:10.1038/s41419-019-1884-7
45. Yang H, Zhang MZ, Sun HW, et al. A novel microcrystalline BAY-876 formulation achieves long-acting antitumor activity against aerobic glycolysis and proliferation of hepatocellular carcinoma. *Front Oncol*. 2021;11:783194. doi:10.3389/fonc.2021.783194
46. Feng H, Zhao L, Bai Z, et al. Aptamer modified Zr-based porphyrinic nanoscale metal-organic frameworks for active-targeted chemo-photodynamic therapy of tumors. *RSC Adv*. 2023;13(16):11215–11224. doi:10.1039/D3RA00753G
47. Wang H, Chen T, Ren H, et al. Metal-organic frameworks@Au nanoreactor as an oxidative stress amplifier for enhanced tumor photodynamic therapy through the alleviation of hypoxemia and the depletion of glutathione. *ACS Appl Bio Mater*. 2023;6(9):3376–3386. doi:10.1021/acsabm.2c01090
48. Yuan H, Chen K, Geng J, Wu Z, Wang C, Shi P. Metal-organic framework PCN-224 combined cobalt oxide nanoparticles for hypoxia relief and synergistic photodynamic/chemodynamic therapy. *Chemistry*. 2024;30(36):e202400319. doi:10.1002/chem.202400319